



Investigation of the non-uniform distribution of current density in commercial-size proton exchange membrane fuel cells

Linfa Peng^{a,*}, Heng Shao^a, Diankai Qiu^a, Peiyun Yi^a, Xinmin Lai^{a,b}

^a State Key Laboratory of Mechanical System and Vibration, Shanghai Jiao Tong University, Shanghai, 200240, PR China

^b Shanghai Key Laboratory of Digital Manufacture for Thin-walled Structures, Shanghai Jiao Tong University, Shanghai, 200240, PR China

HIGHLIGHTS

- A large-area segmented PCB current sensor plate is designed and tested.
- The current distribution of a commercial-size fuel cell stack is investigated.
- Nonuniformity contact pressure has a great impact on current density distribution.

ARTICLE INFO

Keywords:

Commercial-size fuel cell
Printed circuit board
Current density distribution
Assembly condition

ABSTRACT

It is necessary to obtain the current density distribution in order to understand local reactions inside the proton exchange membrane (PEM) fuel cells. Enlarging the active area to commercial-size makes it difficult to maintain uniform assembly pressure, gas supply and heat dissipation inside the fuel cell stack. Existing studies for laboratory-level fuel cells cannot effectively guide the development of large-area fuel cells. In this study, current density distribution inside a 250 cm² and 3 kW level fuel cell stack is measured and analyzed using the printed circuit board (PCB) technology. A four-layer PCB sensor plate covering 144 current collecting segments and shunt resistors for current measurement is well-designed. The in-house developed measurement system is proved with good function, and the accuracy of current density measurement is within 2%. Results show that the flow field configuration and stack assembly condition greatly affects the uniformity of local current densities. Higher current passes through the area with larger contact pressure, and the current density is low in the poor contact area. The local current density has larger deviations for higher output current, but the normalized current is more uniform. Effects of operating conditions including stoichiometric ratio and flow direction are investigated.

1. Introduction

Proton exchange membrane (PEM) fuel cells are being widely applied on power sources for automobiles, unmanned aerial vehicles and stationary power systems of the future owing to their advantages including low pollution, low noise, low operating temperature, high power density and high energy conversion efficiency [1,2]. For high power applications represented by fuel cell vehicles, for example, passenger cars and buses, commercial fuel cell stacks usually need hundreds of cells and large active area for each cell. High-power fuel cell stacks are typically designed with an active area of 150–500 cm² [3–5]. Scaling up the active area from 10 to 50 cm² in laboratory level to commercial size encounters challenges in reaction gas flow distribution, water-heat management, and reaction uniformity. Temperature, reaction gas

concentration, clamping pressure, and current density distribution in large-area fuel cells are more uneven. In the design of commercial large-area fuel cells, it is necessary to consider the coupling relationship of various non-uniform physical quantities for optimizing the flow field, stack structure, and operating condition. For example, the flow field is desired to be appropriately designed to distribute the reactants uniformly and avoid water plugging [6–9]. Otherwise, gas starvation, flooding, and catalyst carbon corrosion may occur due to local uneven distribution.

Conventional fuel cell stack testing methods such as polarization curve measurement can give an overall performance but lack of local information at different positions for the large active area. The current density is directly linked to the electrochemical reaction of fuel cells, so its distribution over the active area provides the local performance in

* Corresponding author.

E-mail addresses: penglinfa@sjtu.edu.cn, penglinfa@sjtu.edu.cn (L. Peng), shaoheng@sjtu.edu.cn (H. Shao).

<https://doi.org/10.1016/j.jpowsour.2020.227836>

Received 5 November 2019; Received in revised form 14 January 2020; Accepted 3 February 2020

Available online 14 February 2020

0378-7753/© 2020 Elsevier B.V. All rights reserved.

energy conversion [10]. Local current density distribution is a function of the local concentration of electroactive species at the electrode surface, as well as the potential distribution in the cell, relating to pressure, relative humidity and temperature [11,12]. Poor current density distribution in the PEM fuel cells could result in poor reactant and catalyst utilization. The uneven current density distribution reduces the energy conversion efficiency of the entire fuel cell. At the same time, uneven current density distribution can cause local hot spots and gas starvation resulting in coating corrosion of the bipolar plate [13], local corrosion of the catalyst [14], or membrane degradation leading to reduced life of the fuel cell [15–18]. Therefore, it is needful to get a good understanding of the current density distribution in the large-area fuel cell.

There are some researchers who focus on experimentally investigating current density distribution inside PEM fuel cells in the last decade. Current density distribution can be determined by applying the segmented cell or by inserting sensor plates into the fuel cells. In such systems, currents are directly measured by means of shunt resistors or Hall effect sensors [19]. For the segmented cell approach, current collectors are usually segmented to form several current collecting terminals or wires isolated from each other. For example, Liu et al. [20] used 12 copper bolts to collect current from the special segmented MEA. Copper bolts are connected to current-viewing resistors and then connected to the electric load together. However, the segmented cell method is only valid when measuring the current density distribution of a single cell or the cell at the end of a fuel cell stack. In comparison, the sensor plate approach has the advantage of measuring any one cell in the fuel cell stack because current can pass through the sensor plate and does not need to be taken out of the fuel cell stack. Ghosh et al. [21] used a thin semi-segmented plate made of expanded graphite which serves as a passive resistor network measurement plate. Lilavivat et al. [16] inserted a current density distribution board between the flow field plate and segmented gas diffusion layer (GDL), and the current is measured by a Hall-effect sensor box. Wieser et al. [22] installed a high-resolution Hall sensor plate with fuel cell stack integration. Sun et al. [23] inserted a measurement gasket between the flow field plate and the GDL, and the current at each sub-area of the fuel cell was measured by current collecting strips on the measuring gasket.

The most widely used sensor plate is the printed circuit boards (PCBs) with an array of shunt resistors. Eckl et al. [24] analyzed a PCB with non-segmented bipolar plates and showed that lateral current between neighboring segments is low. Heuer et al. [25] developed a PCB consisting of a low temperature coefficient shunt resistors matrix with 112 elements to determine the local current densities. Shan et al. [26] used electrochemical impedance spectroscopy and locally resolved current density distribution based on PCB technology to analyze the effects of the micro-porous layer on PEM fuel cell performance. Lin et al. [27] applied the PCB technology to study the current density distribution under the rapid cold start process. Belhadj [10] et al. compared current density distributions of an MEA before and after 500-h current cycling using a test fuel cell integrated with a PCB sensor plate. The PCB technology is a cost-effective approach for mapping the current density distribution within a fuel cell. In addition, the PCB sensor plates have advantages of a high-density sensor array and small thickness.

The above-mentioned experimental studies have mainly focused on current density measurement for the small size single cell, and the influence of material properties and operating conditions on the current distribution is analyzed [23,28,29]. In industrial high-power applications, fuel cells are usually designed with a much larger active area. Enlarging the active area to hundreds of square centimeters makes it difficult to maintain uniform assembly pressure inside the fuel cell stack. At the same time, there are differences in flow rate and temperature of fluids between dozens of coolant channels and gas channels, resulting in an increased non-uniformity in the electrochemical reaction inside the stack. In addition, the design of cathode and anode flow field determines the coolant flow field for the metallic bipolar plate. In some areas, anode and cathode gas channels must be crossed or size-modified locally to

form a complete and effective coolant flow field. Consideration of the coolant flow field may further affect the reaction uniformity. Reaction non-uniformity across the active area makes the average output performance decrease and leads to local heat spots and local flooding. The impact of these factors on small-area fuel cells is not significant. However, they must be considered in the design for large-area fuel cell stacks.

The present study intends to investigate the current density distribution in a commercial-size fuel cell stack and get more information about the complex behavior inside the fuel cell which is useful to the improvement of fuel cell design and determining optimal operating conditions. We have adopted the PCB approach to measuring the current density distribution of a 20-cell stack with 250 cm² active area per cell. The current sensor plate is made of a four-layer PCB with 9 × 16 segmented current collecting pads and shunt resistors. Additional temperature sensors in the PCB can measure the temperature distribution of the bipolar plates. The shunt resistors are corrected with the temperature values. The uniformity of the current density distributions is analyzed in response to the design of the flow channels, assembly condition, and operating conditions. The impact of uneven contact pressure distribution is taken into consideration, and cases of different clamping pressures are discussed. Effects of operating conditions including total current, flow direction, stoichiometric ratio, and relative humidity are investigated.

2. Experiments

2.1. Current density distribution measurement

The PCB sensor plate is fabricated with four conducting layers, two layers on the top and bottom surface for segmented current collecting, and the other two layers inside the epoxy resin plate for current and temperature measurement. The working principle of the sensor is shown in Fig. 1 (a). The top and bottom layers cover the zone matching the active area of the MEA. The zone is divided into 144 insulated segments over a 9 × 16 array as current collecting pads. Each segment has an area of 1.74 cm². These pads on the top and bottom layers are coated with gold, shown in Fig. 1 (b). Current collected by the pad can go into the inner current layer through the vertical vias connecting the top layer and the current layer. Signal wires across the shunt resistors are led out to the outside of the fuel cell. The segment current is obtained by measuring the voltage drop of the shunt resistor on the current layer.

A temperature layer is designed for temperature measurement, which is under the current layer and not connected to the other three layers in the PCB. The slender serpentine wires in the temperature layer are used as thermistors for temperature sensing. The resistance value of each thermistor is about 1 Ω. All the thermistors are connected in series. An external constant current source provides a constant 10 mA direct current to the series-connected thermistors. When the 10 mA excitation current is passed, the heating power of the thermistor is only 10 mW and it will not interfere with the temperature measurement. A voltage drop is therefore generated across each thermistor, and it varies with the local temperatures. Wires connecting to the thermistors are also led to the edge of the sensor plate for voltage acquisition.

The PCB sensor plate is calibrated before experiments. Firstly, the temperature is calibrated at room temperature. For each temperature sensor, the real temperature T is converted from the following equation.

$$T = T_0 + (U_T / U_{T_0} - 1) / \alpha \quad (1)$$

where T is the temperature to be measured, T_0 is the room temperature for calibration, α is the temperature coefficient of the copper layer of the PCB, U_{T_0} and U_T are the voltage across the thermistor at the calibration temperature and measuring temperature, respectively.

The method for the calibration of varying current sensors is used the same as the work of Geske et al. [30], and temperature compensation is added. A calibration current of 0.5 A is applied to the sensor through a

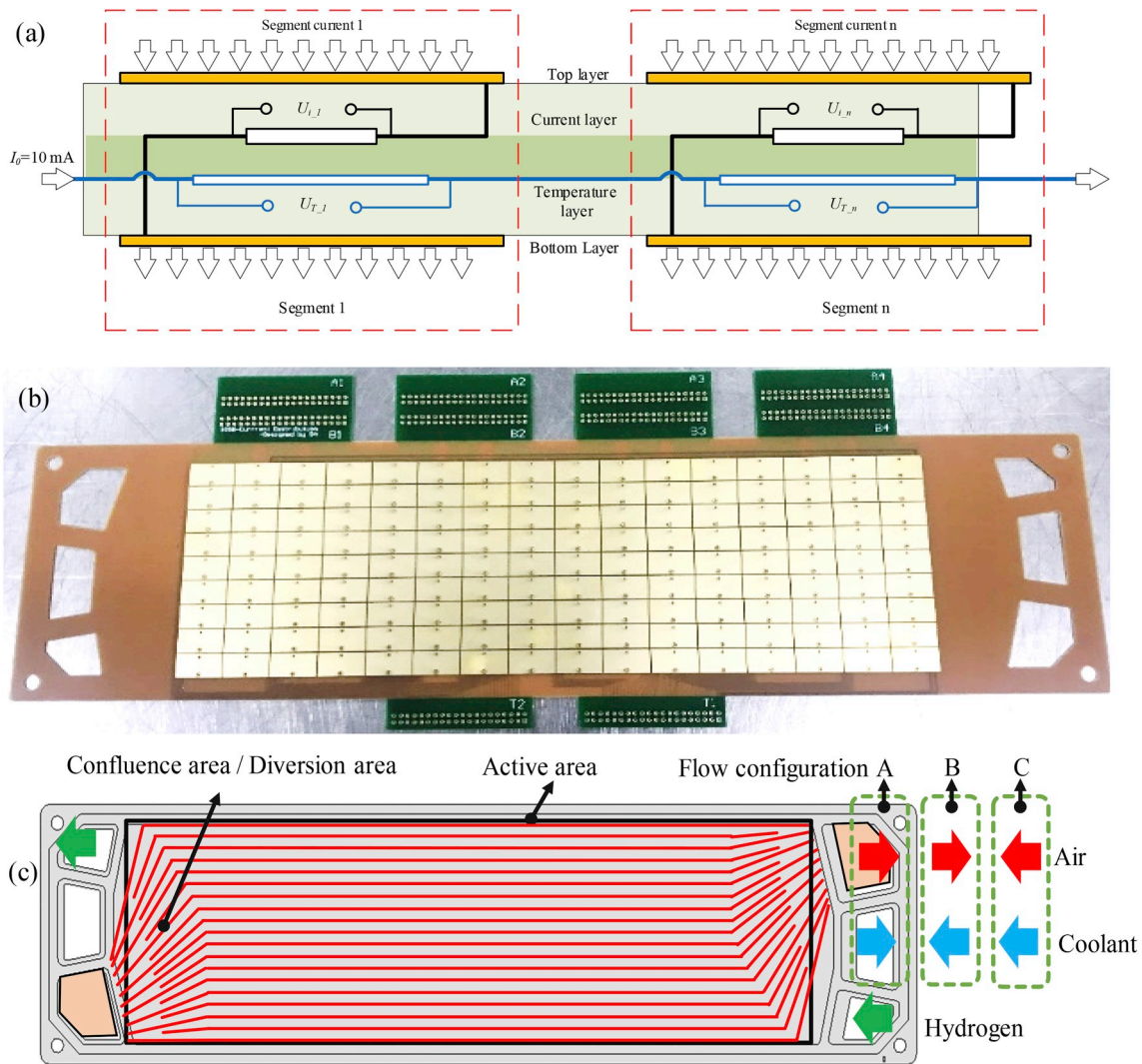


Fig. 1. The schematic diagram of the four-layer PCB (a), the picture of the sensor plate (b) and the schematic diagram of the flow field and flow direction configurations (c).

constant current source, then the voltage across the shunt resistor (U_{i_0}) is recorded. The current density to be measured (i) can be calculated as follows.

$$i = I_0(U_i / U_{i_0}) / (T / T_0) / A \quad (2)$$

where I_0 is the calibration current, U_i is the measuring voltage signal, and A is the segment area.

The accuracy of the sensor plate is tested after calibration, confirming the validity of the measurement device. The temperature measured at any one segment is within $\pm 0.2^\circ\text{C}$ error from the actual temperature measured by an external thermometer. The total current measured over the sensor plate is shown to be within 2% error compared with the current reading from the electronic load. The accuracy of temperature and current measurements can meet the experimental requirements, and measurement results are proved to be reliable.

2.2. Experimental fuel cell stack

Experiments are carried out using commercial metallic bipolar plates for vehicle applications, and the schematic diagram of the flow field is shown in Fig. 1 (c). The bipolar plate is made of two laser-welded stainless steel plates formed with a 0.1 mm thickness substrate. The length and width of the bipolar plate are 408 mm and 107 mm,

respectively. The outlines of the current sensing plate shown in Fig. 1 (b) matches the bipolar plates. The bipolar plate suits for MEA with an active area of 250 cm^2 ($280\text{ mm} \times 89\text{ mm}$). The flow field of the bipolar plate consists of 40 parallel channels for reactant gases contributing to uniform flow distribution for the large-area fuel cell [31]. Coolant channels are inside the bipolar plates. The ribs and channels are both 1.0 mm in width. The cross-section size of these channels is $1.0 \times 0.4\text{ mm}^2$ on the anode and cathode side. A confluence area and a diversion area link these channels together. The reaction gases are injected in the manifolds, in a co-flow or counter-flow configuration.

A seven-layer MEA with a resin gasket is used in the experimental fuel cell. The proton exchange membrane is from GORE. Platinum catalysts of 0.4 mg cm^{-2} and 0.1 mg cm^{-2} are loaded at the cathode and anode, respectively. GDLs with MPLs are used at both electrodes. All the layers in the MEA are not segmented for current distribution measurement.

A 20-cell fuel cell stack is assembled with endplates shown in Fig. 2 (a) - (d). The PCB sensor plate is installed in the middle of the experimental fuel cell, and the PCB is sandwiched by two bipolar plates. We have measured the flow distribution in stacks up to hundreds of cells assembled using the same endplates and metallic bipolar plates to ensure there is no flow distribution problem affecting the current density across the cells. There are two types of assembly methods. For the first method, there are ten disc springs arranged between each bracket and

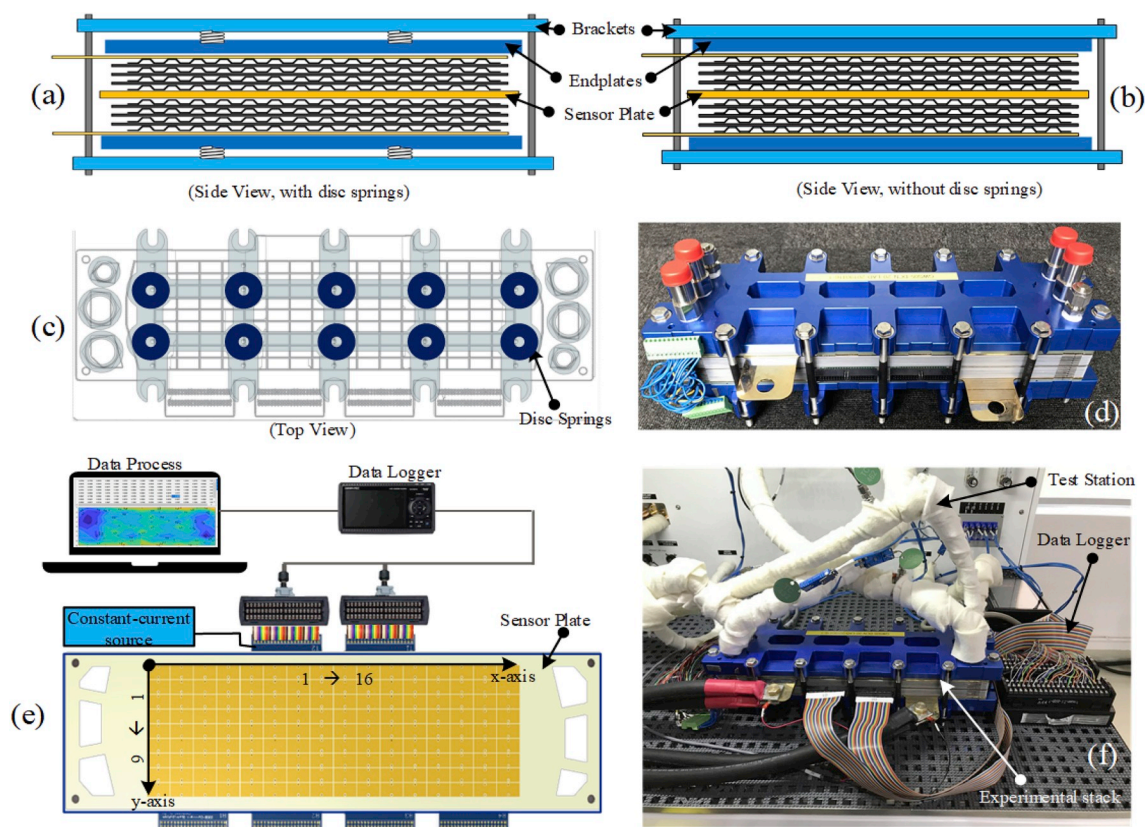


Fig. 2. The schematic diagram of the 20-cell experimental stack from the side view with disc springs (a), the side view without springs (b), the top view (c), the picture of the stack (d), the measuring system (e), and the operating stack on the test station (f).

the endplate to ensure a stable assembly force, shown in Fig. 2 (a) and (c). The clamping force applying on the brackets is transferred to the endplates by the springs. The brackets are fastened with fourteen bolts and tightened with a controlled torque applied at 8 N m per bolt. The material of the bolt is stainless steel 304, the thread diameter is 8 mm, and the thread pitch is 1.25 mm. The disc springs are removed for the second method, shown in Fig. 2 (b).

2.3. Experimental setup

The schematic diagram and the picture of the experimental device are shown in Fig. 2 (e) and (f). Current and temperature density are measured using a system separated from the fuel cell test station. As shown in Fig. 2 (e), The current measuring system consists of a laptop for data processing, a data logger, and a constant current source for temperature measurement. The multi-channel data logger GRAPHTEC GL840 connects the sensor plate. Data on segment current and temperature signals are transferred to the computer. Recorded data is processed by the computer with the data process software coded by MATLAB. The software converts voltage data to real current density and temperature values and realizes the real-time contour map display. The GREENLIGHT G200 fuel cell automate test station is employed to operate the experimental stack. Operating parameters including flow rate, pressure, temperature, and relative humidity are controlled and measured by the test station. Fig. 2 (f) shows the experimental stack operating on the test station.

In the base case experiment, the experimental stack is operated in the standard operating condition, shown in Table 1. The fuel cell is fed with partly humidified air and hydrogen with an inlet relative humidity of 30%. The stoichiometric ratio is equal to 1.5 and 2.4 for hydrogen and air, respectively. Both the anode and cathode gas inlet pressure are set to 100 kPag. The coolant flow rate is set to 0.5 L min^{-1} per cell, and the

Table 1

The standard operating condition.

Media	Inlet pressure (kPag)	Stoichiometric ratio	Dew point ($^{\circ}\text{C}$)	Inlet temperature ($^{\circ}\text{C}$)	Inlet humidity (%RH)
Hydrogen	100	1.5	36	60	30
Air	100	2.4	36	60	30
Coolant	100	–	–	60	–

coolant inlet temperature is 60°C .

Experiments for current and temperature distribution measurements are conducted under steady state. The fuel cell is allowed to run for 600 s under the selected conditions to reach its steady state before recording the current and temperature data. Current and temperature distributions under different assembly pressure, flow directions, and operating conditions are investigated.

3. Distributions in the commercial-size fuel cell stack

The experiment for the 20-cell-stack assembled with disc springs under the standard operating condition illustrates a basic distribution profile of the large-area fuel cell stack. Fig. 3 shows the measurement results for temperature and current density distribution represented in 2-dimensional contour maps in the experimental fuel cell operating at a total current of 250 A. Thus, the average current density is 1.0 A cm^{-2} . The flow direction of coolant and gases are marked with arrows. The position and direction of the coordinate system are shown in Fig. 2 (e).

It should be noted that the measured temperature distribution is close to the temperature of the coolant rather than the temperature inside the gas channels or MEA because the sensor plate is sandwiched between two metallic bipolar plates with coolant circulation. The

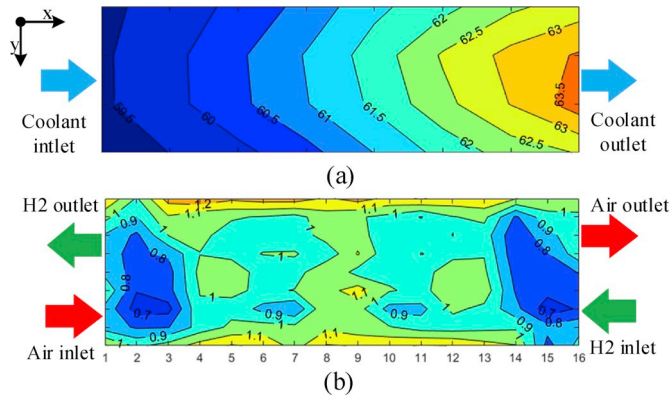


Fig. 3. The temperature (°C) distribution (a) and current density (A cm⁻²) distribution (b) of the stack operating at 250 A current in the standard condition.

temperature distribution in Fig. 3 (a) indicates that the coolant inlet temperature is 59.5 °C, and the deviation from the set value of the test station is within 1 °C. The thermocouple for the test station is installed on the coolant pipeline. Although the coolant pipeline is with heat insulation, there is heat loss and result in a temperature decrease inside the stack. Coolant flow is injected from the left edge of the active area, and it is constantly heated by the cells during the flow to the coolant outlet. The temperature rises to 63.5 °C at the coolant outlet on the right edge. The contour line is convex to the left, indicating that the temperatures of the middle area are higher than the upper and lower edges at the same x-coordinate position.

Results of current density distribution are shown in Fig. 3 (b). When the experimental fuel cell operates at an average current density of 1.0 A cm⁻², the local current densities in the fuel cell are within the range of 0.65–1.28 A cm⁻². The unevenness of the current density can be caused by a variety of factors, including distributions of reactant concentration, temperature, water content and so on.

It can be seen that the local current density does not monotonically

increase or decrease in the x-axis direction. There are three regions with a large current density in the middle. In addition, the current density on the top and bottom edge of the active area is relatively large. This phenomenon is not found in researches for small-area fuel cells. Alefour et al. [29] revealed that the current density is highest in the near inlet region then decreases downstream following the flow and becomes the lowest in the region near the outlet in a 40 cm² fuel cell. Hwnag et al. [32] found a local maximum near the entrance of the flow-field plate, and a local minimum near the outlet of the flow-field plate in a 25 cm² fuel cell. This kind of distribution characteristics in the present work does not appear to be caused by uneven gas supply or water-heat state, presumably due to uneven contact pressure of the large-area fuel cell stack. Contact pressure applied by clamping the endplate of the cell can be insufficient, which may result in poorer performance in this part [33].

In order to verify the above speculation, the contact pressure distribution measurement inside the middle cell of the stack is carried out. When the experimental fuel cell is assembled with an 8 N m torque of each bolt, the image of the FUJIFILM pressure measurement film is shown in Fig. 4 (a). The central and edges of the pressure-sensitive film are darker in color, indicating larger contact pressure in the corresponding area. By scanning the standard color card provided by the manufacturer, the correspondence between the color information and the pressure value is obtained to fit an empirical calibration equation. The scanned image of the film is binarized. The color value of each pixel on the pressure-sensitive film after compression is converted into a pressure value by the pressure calibration equation. Then we perform a localized averaging process to blur the differences between the ribs and channels to obtain the nominal contact pressure on the MEA. The contact pressure values of the same x-coordinate are averaged to obtain a statistical pressure curve along the x-axis direction shown in Fig. 4 (c). The current density distribution from Fig. 4 (b) is also averaged, and the current density curve along the x-axis direction is shown in Fig. 4 (d).

The flow fields are parallel to the x-coordinate, the gradient of species and temperature are greater along this direction. Comparing Fig. 4 (c) and (d), contact pressure distribution and the current density have a similar profile with five equally spaced maximum locations. The

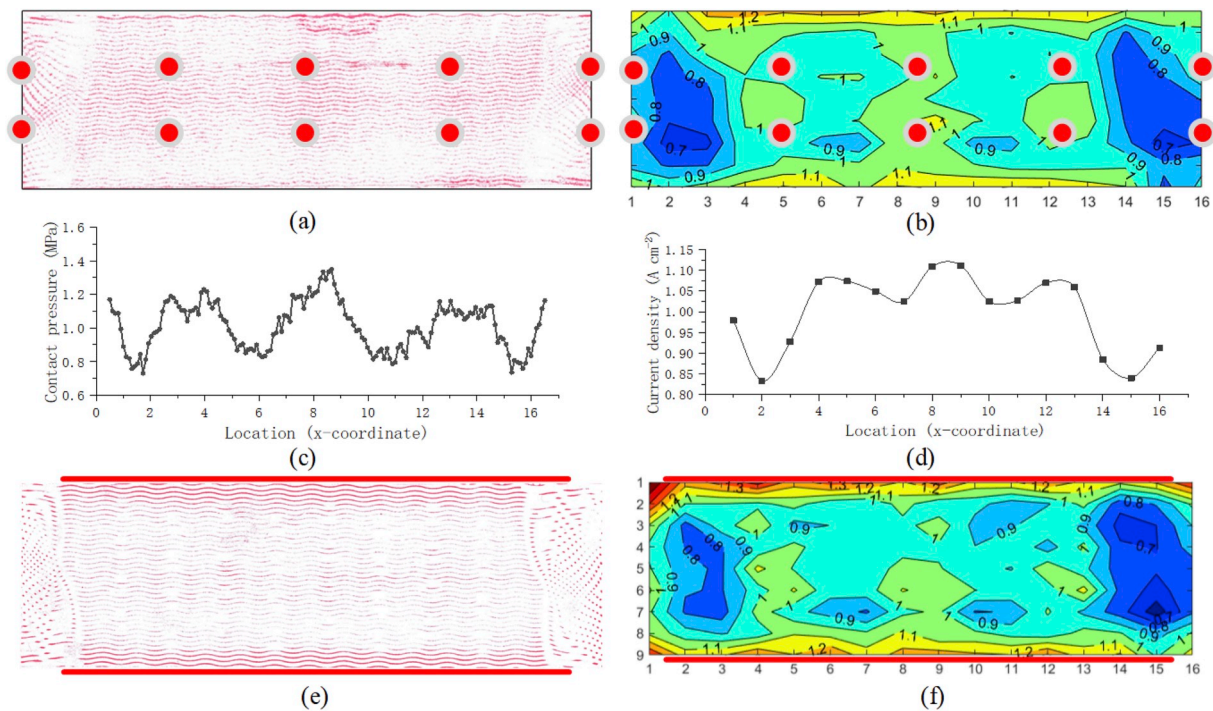


Fig. 4. The contact pressure distribution (a, c) and the current density distribution (b, d) in the 20-cell stack with disc springs; the contact pressure distribution (e) and the current density distribution (f) in the 20-cell stack without disc springs.

locations of disc springs are marked with red dots in Fig. 4 (a) and Fig. 4 (b). The area where the contact pressure and current density is large corresponds to the arrangement position of the bolts and disc springs. The bracket transmits clamping force to the endplates through the springs. Due to the slight deformation of the endplates, the contact pressure in the stack core is not uniform. The area near the load points has relative high contact pressure.

Due to the high conductivity of metallic bipolar plates, it is overall equipotential in the bipolar plates although there may be a local potential difference. The bulk and contact ohmic resistance play an important role in affecting the potential in the catalyst layers. Qiu et al. [34] experimentally studied the relationship between the contact pressure and the contact resistance. Lin et al. [35] measured the through-plane resistance of the GDL. According to their studies, both the contact and bulk resistance decreases as the contact pressure increases. Thus, local over-potential and reaction rate on the catalyst layers are influenced by local electrical resistance. At the position where the contact pressure is higher, the resistance of the GDL and its interface is lower, leading to more current passing through. It can be seen that the current density in fuel cells is sensitive to local electric resistance distribution.

In the large-area fuel cell, the arrangements of gas channels in different areas may be different, considering the gas/coolant distribution and manifold placement. The flow field design has an impact on the contact pressure and current density distribution. The flow field on the metal bipolar plate in the present work is shown in Fig. 5 (a). After the gas enters from the manifold, it is diverted to the parallel flow channel area through the diversion area, then re-aggregated in the confluence area, and finally reaches the outlet manifold. As shown in Fig. 5 (b), a crossflow is formed in the diversion area for the reason that the anode and cathode flow direction is not parallel. In the central active area, the anode and cathode flow channels are parallel and completely coincident, as shown in Fig. 5 (c). Only in the regions where the ribs of the cathode and anode coincide, the MEA will be compressed to the desired thickness. In the crossflow regions, for the MEA, one side contacts the channel and the other side contacts the rib, and the contact pressure at these areas is quite small. When the anode and cathode channels cross, the effective contact area is smaller than that for the parallel channels. The average contact pressure or nominal contact pressure is also smaller when the GDL compression ratio is the same. So, the contact pressure in the confluence area and the diversion area is insufficient, resulting in lower local current density.

The contact pressure distribution and current density distribution are also sensitive to the stack assembly method. For comparison, the 20-cell-stack is assembled without disc springs. In the fuel cell stack without disc springs, the bolt force deforms the brackets, and the directly contacted endplate is also bent under the clamping pressure. The deformation displacement at the edge of the endplate is larger than in the middle,

resulting in larger contact pressure at the edge of the active area. It can be seen from the pressure measurement film in Fig. 4 (e) that the four or five channels on the edges are in a darker color than the others. The measurement of the current density distribution in the 20-cell-stack without disc spring is given in Fig. 4 (f). The current density in the edge area exceeds 1.3 A cm^{-2} , and the standard deviation of the current density is 0.19 A cm^{-2} . In the stack with disc springs, the maximum current density at the edge is only 1.1 A cm^{-2} , and the standard deviation of the current density is 0.15 A cm^{-2} . Installing disc springs on the endplates can uniformly distribute the clamping force to the active area while improving the uniformity of the internal current density distribution. So, assembling the stack with springs is a better method, and springs are used in the following experiments.

4. Results and discussion

4.1. Effects of clamping force

In order to further study the influence of stack assembly conditions on the internal current density distribution. Different tightening torques of bolts are applied for clamping the experiment fuel cell stack. Current density measurements are conducted when the torque is 4 N m, 6 N m, and 8 N m, respectively. Fig. 6 (a) - (c) shows the contour maps of current density distribution increasing the torque from 4 N m to 8 N m. The area of current density over 1.1 A cm^{-2} and less than 0.8 A cm^{-2} shrinks as increasing the torque. The current density trend along the x-axis direction at different torques are compared and shown in Fig. 6 (d). The averaged current density at the location where the x-coordinate is 2 rises from 0.72 A cm^{-2} at 4 N m to 0.93 A cm^{-2} at 8 N m. It can be concluded that current density distribution uniformity gets better as increasing the clamping force.

Shape error of thin metallic plates is not avoidable due to its flexibility and springback in the stamping process, as well as deformation resulted from thermal stress in the welding process. In the process of clamping the stack, the central part of the active area is compressed firstly due to the overall warping deformation of bipolar plates. So when the clamping force is low, most current flow through the central area due to low contact resistance. When gradually increasing the clamping force, the outside area gets larger pressure and diverts more current. Therefore, the total current density distribution gets more uniform, the standard deviation decreases from 0.16 A cm^{-2} to 0.12 A cm^{-2} . At the same time, the average output voltage per cell of the stack shows an increase from 0.643 V at 4 N m, 0.665 V at 6 N m to 0.677 V at 8 N m. The performance improvement comes from lower contact resistance due to better contact conditions of MEA and bipolar plates. It should be noted that too high assembly pressure will lead to the low porosity of GDL in which case that the liquid water is difficult to be drained out of the GDL, and reactants are also difficult to diffuse into the catalyst layer.

4.2. Effects of flow configuration

Flow direction configuration of hydrogen, air, and coolant has a significant influence on heat and water distribution in fuel cell stacks. The flow direction of the coolant determines the temperature gradient direction in the fuel cell stack. The coolant absorbs the heat generated by the stack and the temperature increases along the direction of the coolant flow. Co-flow and counter-flow configuration of hydrogen and air affects the humidity distribution of the reactant, resulting in a difference in the water content of the PEM. The experimental fuel cell has a parallel flow field for the hydrogen, air, and coolant, and the inlet and outlet of each fluid can be exchanged to investigate the effects of flow direction configuration.

Firstly, we experimentally confirmed that the coolant flow indeed affects the current density distribution. The current density distribution under the standard condition with flow configuration A has already been shown in Fig. 3 (b). Based on the standard operating condition, the

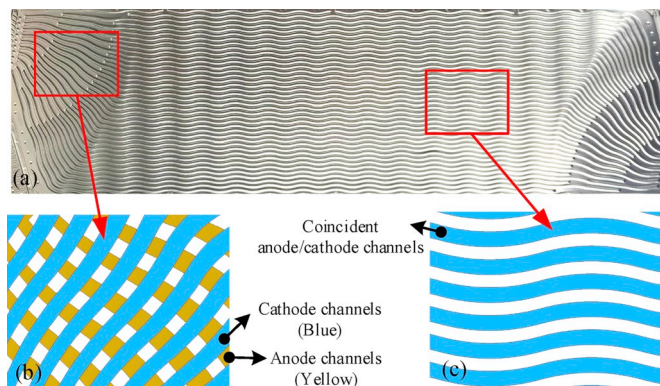


Fig. 5. The picture of the flow field (a), and the gas channels in the confluence/diversion area (b) and the central active area (c).

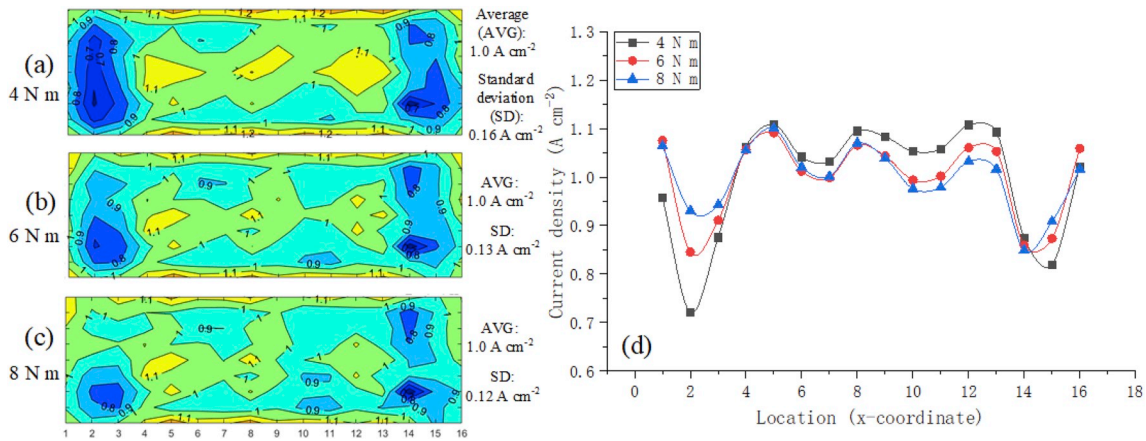


Fig. 6. Current density distribution with a torque of 4 N m (a), 6 N m (b), 8 N m (c) and curves along the x-axis (d).

coolant flow rate is reduced to 0.3 L min^{-1} , and the inlet temperature is set to 70°C . The temperature difference between the coolant inlet and outlet reaches 7°C at this time. The current density distribution at a total current of 250 A is shown in Fig. 7 (a). The current density in the left region is lower because of the lower water content at higher temperatures and results in proton conductivity decrease. Compared with the standard condition, the current density distribution shows an increase in the central area of the active area as the coolant temperature is increased.

Then we investigated the effects of flow configuration on the cell performance and current density distribution. The current density distributions measured in different flow directions are compared in Fig. 7. For configuration B and C, the inlet temperature is all set to 70°C . Fig. 7 (b) and (c) shows the contour maps in flow configuration B and C. The flow configuration A has the most uniform current density distribution, and the average cell voltage is 0.682 V. The standard deviation of current density is 0.16 A cm^{-2} , 0.20 A cm^{-2} and 0.19 A cm^{-2} for flow configuration A, B and C, respectively. In flow configuration A, the inlet relative dry air faces the hydrogen outlet where hydrogen is fully humidified. Flow configuration B and C show more non-uniform current density distribution due to local membrane drought. The rectangular lines on the map identify the area where the current density is small, that is, the area where the membrane is dry. The average cell voltage is

0.652 V and 0.650 V for flow configuration B and C, respectively. In flow configuration B, the flow direction of coolant is opposite to the direction in configuration A, and the hydrogen and air are counter-flow. It can be seen that the current density on the left side decreases compared with flow configuration A. The cathode is the water generating electrode, and the humidity distribution of the air plays a key role in the distribution of water content in the membrane. The coolant outlet and air inlet are both on the left side. Air near the inlet contains little water, and the temperature is highest. As a result, the membrane in the left area is dehydrated, resulting in low local current density. In flow configuration C, hydrogen, air, and coolant are all in co-flow direction. The membrane on the right side is dehydrated because the air and hydrogen just flow into the flow field, and there is not enough water to humidify the membrane. The above results show that flow configuration has a great influence on water-heat management and should be carefully considered in fuel cell design. Air-hydrogen counter-flow and air-coolant co-flow configuration ensures high water content in all areas for the PEM and achieves the best performance for the fuel cell stack in the present work.

4.3. Effects of operating condition

Current, cathode and anode stoichiometric ratio and relative humidity are selected as variables to study the effects of operating conditions. The total current of 250 A and the standard operating condition in Table 1 is used as base parameters. All the experiments investigating the effects of the total current, stoichiometric ratios, and relative humidity are conducted controlling the corresponding single variable.

Effects of total current from 50 to 250 A (average current density $0.2\text{--}1.0 \text{ A cm}^{-2}$) on the current density distribution are investigated. The local current density for the total current of 50 A, 150 A and 250 A are drawn as 3-dimensional surface maps in Fig. 8 (a). The uniformity of current density in 50 A case is best. Larger total current contributes to a larger distribution range of local current density. Histograms for local current density are shown in Fig. 8 (b). As the total current increases, the range of current density becomes larger.

The data of local current density for different total current is normalized, and the normalized current density along the x-axis direction is shown in Fig. 8 (c). Although the absolute distribution deviation of the local current density is small at low current, the normalized distribution appears uneven. The coefficient of variation is used to compare the uniformity of current distribution of cases under different currents. The coefficient of variation is 22%, 18%, 17%, 16% and 15% for the case with a current of 50 A, 100 A, 150 A, 200 A and 250 A, respectively. In the same operating condition, for the case of 100 A current, the fuel cell itself generates little water, and the water is insufficient to wet the PEM. Especially in the area of the air inlet, the proton conductivity of the membrane is at a low level, resulting in decreased current density and a

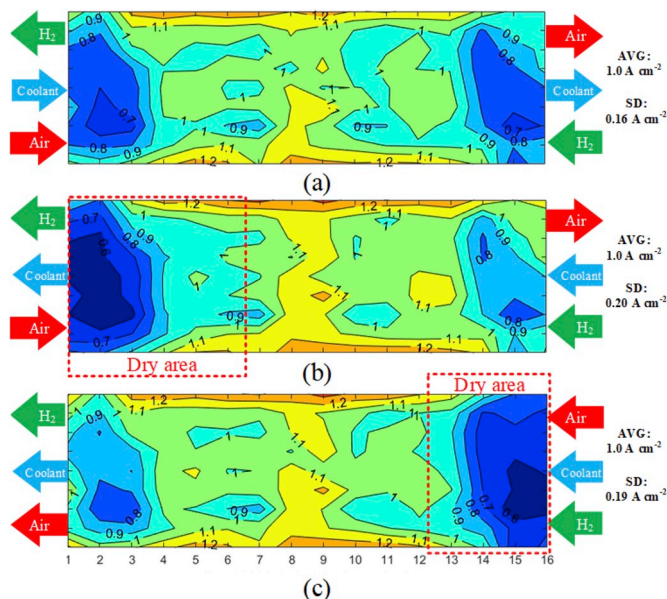


Fig. 7. Current density distribution in flow configuration A (a), B (b), and C (c).

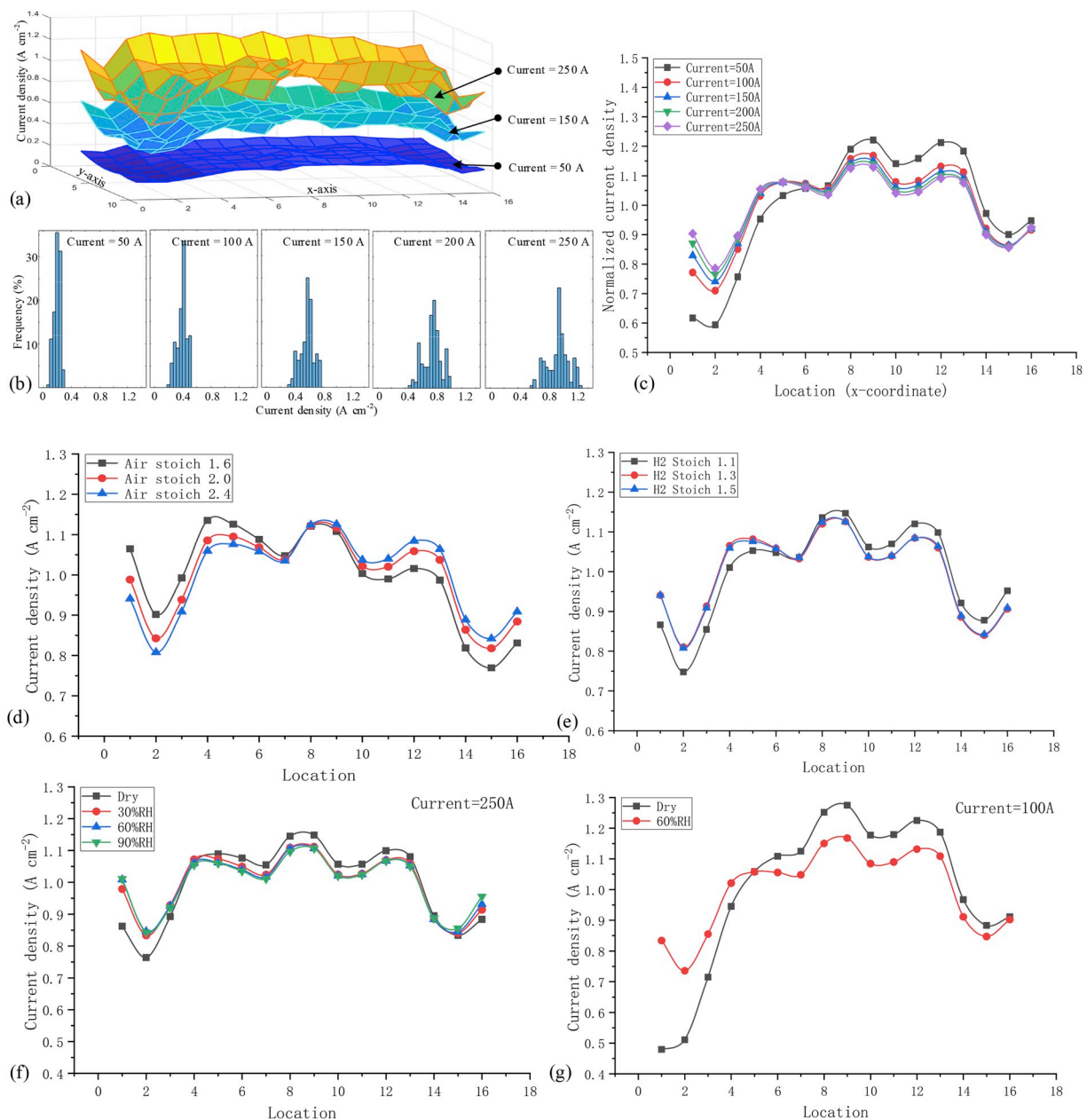


Fig. 8. The surface map of current density (a), histogram of current density distribution (b), and normalized current density distribution (c) under different total currents; effects of air (d) and hydrogen (e) stoichiometric ratio at 250 A current; effects of relative humidity at 250 A (f) and 100 A (g) current.

more uneven current density distribution throughout the active area. As total current increases, the membrane drought relieves with the contribution of more generating water.

Decreasing the air stoichiometric ratio significantly affects the local oxygen partial pressure in the downstream of air channels. The range of local current density shows an increasing trend as the air stoichiometric ratio decreases, shown in Fig. 8 (d). The average cell voltage is 0.657 V, 0.669 V and 0.677 V with an air stoichiometric of 1.6, 2.0, and 2.4, respectively. Higher fuel cell output voltage is obtained in the case with a higher air stoichiometric ratio. The effect of the stoichiometric ratio of hydrogen is also experimentally studied. The results in Fig. 8 (e) show that the current density distribution is nearly unchanged when modifying the hydrogen stoichiometric ratio from 1.5 to 1.3. In these situations, fuel cell performance shows only a tiny change from 0.679 V to 0.676 V. The fuel cell performance is not sensitive to the hydrogen flow rate. However, hydrogen starvation occurs while the hydrogen stoichiometric ratio is reduced to 1.1. In the case with an extremely low

hydrogen stoichiometric ratio, the reaction in the hydrogen outlet area slows down, thus the local current density is decreased. The output voltage is reduced to 0.655V. So, the optimum condition for the hydrogen stoichiometric ratio is 1.3 achieving no starvation and high hydrogen utilization ratio.

In order to analyze the effects of water content in reactants, we have measured the current density distribution at a total current of 250 A for varying gas inlet humidification, as shown in Fig. 8 (f). There is no significant difference in current density distribution when increasing the inlet relative humidity of air and hydrogen from 30% to 90%. However, if the gases are not humidified, the current density in the left side (air inlet area) drops sharply, and the current density near the right side (air outlet area) increases. In the case of a total current of 100 A shown in Fig. 8 (g), the current density distribution in the dry gas condition shows a greater difference than in the 250 A case. The reason is that the electrochemical reaction produces less water at low current, and the membrane drought is more serious. Therefore, for the fuel cell stack in

the pressure work, gas humidification is necessary, and the relative humidity around 30–60% is sufficient.

5. Conclusion

In the present study, the current density distribution of a large-area PEM fuel cell stack is obtained by using the PCB current measurement technology. The 3-kW level 20-cell fuel cell with an active area of 250 cm² is integrated with an in-house made PCB sensor plate. The current measurement data is temperature compensated and calibrated. Verification experiments are carried out to make sure that the local current measurement system works with good accuracy.

The current density distributions are illustrated under different stack assembly and operating conditions. It is found that the current distribution acquired in the large-area stack is sensitive to non-uniform contact pressure, water-heat state and gas supply conditions, and the following conclusions can be drawn:

- (1) The current distribution characteristics are related to contact pressure distribution in large-area fuel cell stacks. More current passes through the area with concentrated contact pressure, and the current density is low in the poor contact area. Assembly with disc springs and increased torque of bolts helps to improve the current distribution uniformity. The current density in the confluence/diversion area is lower than that in the middle active area due to the cross-flow design.
- (2) The flow directions of hydrogen, air, and coolant affect the water-heat distribution inside the stack. The configuration of the air-coolant counter-flow or air-hydrogen co-flow will cause high temperature and low humidity in a specific area of the PEM, resulting in low water content and proton conductivity. Hence, the dry region of the membrane leads to an uneven current density, which lowers the performance of the fuel cell.
- (3) When the fuel cell is operated at the lower total current, the difference in local current densities is smaller. The dispersion of current density distribution at higher currents is larger. It is found that the normalized current density distribution at low currents is rather uneven due to less water production.
- (4) The current density distribution is more sensitive to the flow rate of air than that of hydrogen, and local gas starvation occurs when the hydrogen stoichiometric ratio is 1.1. Gas humidification significantly improves stack performance and current density uniformity when the fuel cell is operated at low current.

The results obtained from the measurement of current density provide guidance for commercial-size PEM fuel cell design and water-heat management. In future work, we look forward to introducing the partitioned impedance measurement technique to analyze the local impedance information in the PEM fuel cell stack. Also, the contact pressure and cooling condition may be different in the edge cells in the stack, the edge effect is necessary to be considered in the long stack in the following study.

Declaration of competing interest

The authors declare that they have no known competing financial

interests or personal relationships that could have appeared to influence the work reported in this paper.

Acknowledgments

This work was supported by the National Key Research and Development Program of China (2017YFB0102803) and National Natural Science Foundation of China (No. 51705308 and 51975363).

References

- [1] C.Y. Wang, Chem. Rev. 104 (2004) 4727–4765.
- [2] T. Kotaka, Y. Tabuchi, U. Pasaogullari, C.-Y. Wang, Electrochim. Acta 146 (2014) 618–629.
- [3] S. Shimpalee, S. Greenway, D. Spuckler, J.W. Van Zee, J. Power Sources 135 (2004) 79–87.
- [4] S. Shimpalee, S. Hirano, M. DeBolt, V. Lilavivat, J.W. Weidner, Y. Khunatorn, J. Electrochem. Soc. 164 (2017) E3073–E3080.
- [5] G. Zhang, X. Xie, B. Xie, Q. Du, K. Jiao, Int. J. Heat Mass Tran. 130 (2019) 555–563.
- [6] Y. Xu, L. Peng, P. Yi, X. Lai, Int. J. Hydrogen Energy 41 (2016) 5084–5095.
- [7] L. Peng, J. Mai, P. Hu, X. Lai, Z. Lin, Renew. Energy 36 (2011) 1413–1420.
- [8] R.B. Ferreira, D.S. Falcão, V.B. Oliveira, A.M.F.R. Pinto, Energy 82 (2015) 619–628.
- [9] D. Qiu, P. Yi, L. Peng, X. Lai, Int. J. Hydrogen Energy 38 (2013) 6762–6772.
- [10] M. Belhadj, A. Aquino, J. Heng, S. Kmiotek, S. Raël, C. Bonnet, F. Lapicque, Chem. Eng. Sci. 185 (2018) 18–25.
- [11] D. Pletcher, F.C. Walsh, Industrial Electrochemistry, Springer Science & Business Media, 2012.
- [12] K. Takanohashi, T. Suga, M. Uchida, T. Ueda, Y. Nagumo, J. Inukai, H. Nishide, M. Watanabe, J. Power Sources 343 (2017) 135–141.
- [13] F. Bi, P. Yi, T. Zhou, L. Peng, X. Lai, Int. J. Hydrogen Energy 40 (2015) 9790–9802.
- [14] S.J.C. Cleghorn, C.R. Derouin, M.S. Wilson, S. Gottesfeld, J. Appl. Electrochem. 28 (1998) 663–672.
- [15] J. Hwang, D. Wang, N. Shih, J. Power Sources 141 (2005) 108–115.
- [16] V. Lilavivat, S. Shimpalee, J.W. Van Zee, H. Xu, C.K. Mittelstaedt, Electrochim. Acta 174 (2015) 1253–1260.
- [17] D. Úbeda, P. Cañizares, M.A. Rodrigo, F.J. Pinar, J. Lobato, Int. J. Hydrogen Energy 39 (2014) 21678–21687.
- [18] D. Úbeda, F.J. Pinar, D.C. Orozco, P. Cañizares, M.A. Rodrigo, J. Lobato, J. Appl. Electrochem. 42 (2012) 711–718.
- [19] M. Schulze, E. Gülzow, S. Schönbauer, T. Knöri, R. Reissner, J. Power Sources 173 (2007) 19–27.
- [20] Z. Liu, Z. Mao, B. Wu, L. Wang, V.M. Schmidt, J. Power Sources 141 (2005) 205–210.
- [21] P.C. Ghosh, T. Wüster, H. Dohle, N. Kimiaie, J. Mergel, D. Stolten, J. Power Sources 154 (2006) 184–191.
- [22] C. Wieser, A. Helmbold, E. Gülzow, J. Appl. Electrochem. 30 (2000) 803–807.
- [23] H. Sun, G. Zhang, L.-J. Guo, H. Liu, J. Power Sources 158 (2006) 326–332.
- [24] R. Eckl, R. Grinzinger, W. Lehnert, J. Power Sources 154 (2006) 171–179.
- [25] M. Heuer, P. Bernstein, M. Wenske, Z. Styczynski, Energies 6 (2013) 3841–3858.
- [26] J. Shan, R. Lin, X. Chen, X. Diao, Int. J. Heat Mass Tran. 127 (2018) 1076–1083.
- [27] R. Lin, Y. Weng, X. Lin, F. Xiong, Int. J. Hydrogen Energy 39 (2014) 18369–18378.
- [28] M. Noponen, T. Mennola, M. Mikkola, T. Hottinen, P. Lund, J. Power Sources 106 (2002) 304–312.
- [29] I. Alaefour, G. Karimi, K. Jiao, S.A. Shakhshir, X. Li, Electrochim. Acta 56 (2011) 2591–2598.
- [30] M. Geske, M. Heuer, G. Heideck, Z.A. Styczynski, Energies 3 (2010) 770–783.
- [31] W. Zhang, P. Hu, X. Lai, L. Peng, J. Power Sources 194 (2009) 931–940.
- [32] J. Hwnag, W. Chang, R. Peng, P. Chen, A. Su, Int. J. Hydrogen Energy 33 (2008) 5718–5727.
- [33] R. Vijayakumar, T. Ramkumar, S. Maheswari, P. Sridhar, S. Pitchumani, Electrochim. Acta 90 (2013) 274–282.
- [34] D. Qiu, L. Peng, P. Yi, X. Lai, Int. J. Mech. Sci. 124–125 (2017) 37–47.
- [35] J.-H. Lin, W.-H. Chen, Y.-J. Su, T.-H. Ko, Fuel 87 (2008) 2420–2424.